Actomyosin stress fiber subtypes have unique viscoelastic properties and roles in tension generation

Stacey Lee[a,b], Elena Kassianidou[a,b], and Sanjay Kumar[a,b,c,*]
[a]UC Berkeley-UCSF Graduate Program in Bioengineering, [b]Department of Bioengineering, and [c]Department of Chemical and Biomolecular Engineering, University of California, Berkeley, Berkeley, CA 94720-1762

ABSTRACT **Actomyosin stress fibers (SFs) support cell shape and migration by directing intracellular tension to the extracellular matrix (ECM) via focal adhesions. Migrating cells exhibit three SF subtypes (dorsal SFs, transverse arcs, and ventral SFs), which differ in their origin, location, and ECM connectivity. While each subtype is hypothesized to play unique structural roles, this idea has not been directly tested at the single-SF level. Here, we interrogate the mechanical properties of single SFs of each subtype based on their retraction kinetics following laser incision. While each SF subtype bears distinct mechanical properties, these properties are highly interdependent, with incision of dorsal fibers producing centripetal recoil of adjacent transverse arcs and the retraction of incised transverse arcs being limited by attachment points to dorsal SFs. These observations hold whether cells are allowed to spread freely or are confined to crossbow ECM patterns. Consistent with this interdependence, subtype-specific knockdown of dorsal SFs (palladin) or transverse arcs (mDia2) influences ventral SF retraction. These altered mechanics are partially phenocopied in cells cultured on ECM microlines that preclude assembly of dorsal SFs and transverse arcs. Our findings directly demonstrate that different SF subtypes play distinct roles in generating tension and form a mechanically interdependent network.**

Monitoring Editor
Yu-Li Wang
Carnegie Mellon University

Received: Feb 15, 2018
Revised: Jun 4, 2018
Accepted: Jun 15, 2018

INTRODUCTION

Cell migration is a critical process in embryogenesis, wound healing, and cancer progression (Friedl and Wolf, 2003; Friedl and Gilmour, 2009). The actomyosin network plays important roles in maintaining a polarized cell shape during migration and mechanosensing by dynamically remodeling and by coordinating the generation and release of tension (Lee and Kumar, 2016). Cells can generate these tensile forces by assembling stress fibers (SF), which are actin-based bundles that frequently contain nonmuscle myosin II (NMII) and are held together by cross-linking proteins such as α-actinin and filamin (Blanchoin *et al.*, 2014; Kassianidou and Kumar, 2015). In addition to forming a three-dimensional network within the cell, many SFs terminate in cell–extracellular matrix (ECM) focal adhesions (FAs), providing a mechanism to directly sense and transmit force between the cytoskeleton and ECM (Burridge and Wittchen, 2013). While SFs have long been appreciated for their role in stabilizing shape and driving motility on rigid two-dimensional ECMs, advances in imaging now reveal that SFs critically regulate migration in both fibrous three-dimensional matrices (Gateva *et al.*, 2014; Owen *et al.*, 2017) and tissue (Hayes *et al.*, 1999; Caspani *et al.*, 2006).

Observations that SFs within a single cell can differ in their location, protein composition, and connections to FAs has led to the classification of SFs into three subtypes: dorsal SFs, transverse arcs, and ventral SFs (Small *et al.*, 1998; Hotulainen and Lappalainen, 2006). Dorsal SFs are oriented perpendicularly to the leading edge of the cell and are anchored at one end to an FA. The other end extends upward (dorsally) and interacts with transverse arcs, which are curved SFs that run parallel to the leading edge and are not anchored directly to FAs. Ventral SFs are located more posteriorly

This article was published online ahead of print in MBoC in Press (http://www.molbiolcell.org/cgi/doi/10.1091/mbc.E18-02-0106) on June 21, 2018.
The authors declare no conflicts of interest.
*Address correspondence to: Sanjay Kumar (skumar@berkeley.edu).
Abbreviations used: ECM, extracellular matrix; FA, focal adhesion; KD, knockdown; KV, Kelvin–Voigt; NMII, nonmuscle myosin II; NT, nontargeting; ppMLC, diphosphorylated myosin light chain; SF, stress fiber.

and are anchored at both ends to FAs (Cramer *et al.*, 1997; Small *et al.*, 1998). In addition to their varied spatial localization, the three subtypes also differ in their molecular composition and mechanism of formation. Dorsal SFs do not contain NMII and are formed by vectoral actin polymerization (Hotulainen and Lappalainen, 2006). On the other hand, transverse arcs and ventral SFs contain NMII clusters, which alternate with cross-linking proteins in a sarcomeric banding pattern. Transverse arcs form from the annealing of Arp2/3-nucleated filaments with mDia2-tropomyosin fragments (Tojkander *et al.*, 2011). Ventral SFs may form de novo from the bundling of short actin filaments (Machesky and Hall, 1997; Vallenius, 2013) or from the fusion of dorsal SF-flanked transverse arcs during retrograde flow of the SF network (Hotulainen and Lappalainen, 2006). During retrograde SF flow, dorsal SFs direct transverse arcs toward the bottom (ventral) surface of the cell, eventually fusing with transverse arcs to form a ventral SF (Hotulainen and Lappalainen, 2006; Tojkander *et al.*, 2015). Ventral SFs generate and transmit significant traction forces that detach the trailing end of the cell after protrusion of the leading edge, facilitating motility (Soiné *et al.*, 2015; Burridge and Guilluy, 2016).

A core concept of prevailing models of cell mechanics is that cells establish shape homeostasis by actively rearranging a prestressed, mechanically interdependent network, with SFs and other contractile elements contributing tension (Ingber, 2003). To this end, there have been several efforts to dissect contributions of specific SF subtypes in generating and maintaining tension, particularly in the context of motility. For example, live-cell imaging and traction force measurements have been elegantly combined to develop a model for the structure of the lamella in which transverse arcs collectively pull on dorsal SFs, which act as levers that flatten the lamella (Burnette *et al.*, 2014). Model-based traction force microscopy, in which cable network models are used to iteratively deduce SF tension from SF and FA distributions, also hints that ventral SFs bear greater tension than the other two subtypes (Soiné *et al.*, 2015). While these studies have produced important new insights into the field's understanding of SF subtype function, they remain indirect measures of SF mechanical properties. Given the central roles that specific SF subtypes are hypothesized to play in cell structure and motility, there is a significant unmet need to directly and comparatively measure mechanical properties of individual SFs of each defined subtype.

We and others have used laser nanosurgery to selectively cut single ventral SFs in live cells and thereby quantify SF mechanical properties and contributions to cell shape and traction (Kumar *et al.*, 2006; Colombelli *et al.*, 2009; Chang and Kumar, 2013; Kassianidou *et al.*, 2017a,b). On incision, SFs release their stored tension, which is experimentally observable through the retraction of the two severed ends of the SF. The retraction kinetics can be interpreted in terms of SF prestress and viscoelasticity by modeling the SF as a Kelvin–Voigt (KV) material composed of parallel springs and dashpots (Kumar *et al.*, 2006; Tanner *et al.*, 2010; Chang and Kumar, 2015). Using these tools, it has been found that peripherally located ventral SFs are under higher prestress than centrally located ventral SFs. Furthermore, compromise of a single peripheral (but not central) ventral SF substantially destabilizes cell morphology (Kumar *et al.*, 2006; Tanner *et al.*, 2010). More recently, we showed that the degree of myosin regulatory light chain (MLC) phosphorylation along central and peripheral ventral SFs are preferentially regulated by Rho-associated kinase (ROCK) and myosin light chain kinase (Tanner *et al.*, 2010; Kassianidou *et al.*, 2017b). The degree with which an SF is physically networked with other SFs can also influence the retraction, by slowing or enhancing retraction depending on network architecture and geometry, and by serving as repositories for the released tension that mitigate destabilization of adhesions (Chang and Kumar, 2013; Kassianidou *et al.*, 2017a).

In this study, we apply laser nanosurgery to directly and systematically measure the viscoelastic properties and structural contributions of dorsal SFs, transverse arcs, and ventral SFs. Each subtype exhibits distinct mechanical properties, with ventral SFs bearing the greatest prestress. Genetic depletion of transverse arcs and dorsal SFs further reveals that ventral SF mechanics depend on the presence of the other two subtypes, a finding that is reinforced by studies on patterned one-dimensional matrix substrates. Together our results support a model in which the three SF subtypes form a physically and mechanically integrated network in which the contractile properties of ventral SFs are related to and derived from dorsal SFs and transverse arcs.

RESULTS

Dorsal SFs bear the least prestress and are mechanically coupled to transverse arcs

We focused our studies on U2OS osteosarcoma cells, which assemble robust SF networks and are widely employed as a model system for investigating SF function (Hotulainen and Lappalainen, 2006; Burnette *et al.*, 2014; Gateva *et al.*, 2014; Tojkander *et al.*, 2015). Consistent with previous observations, we found that U2OS cells displayed dorsal, transverse arc, and ventral SF subtypes, which we distinguished based on their connections to vinculin in FAs and their location within the cell (Figure 1A, left). SF subtypes also had distinct patterns of diphosphorylated MLC (ppMLC) staining, the form of MLC typically associated with high SF contractility (Ikebe *et al.*, 1988; Chrzanowska-Wodnicka, 1996; Vicente-Manzanares and Horwitz, 2010). Dorsal SFs were devoid of ppMLC, whereas transverse arcs and ventral SFs had punctate ppMLC staining along the length of the fibers (Figure 1A, right), suggesting that dorsal SFs are not intrinsically tensed, whereas transverse arcs and ventral SFs are (Hotulainen and Lappalainen, 2006; Tojkander *et al.*, 2011; Burnette *et al.*, 2014; Tee *et al.*, 2015). To test this prediction, we applied laser nanosurgery to sever SFs within each of the subtypes in live cells to measure elastic prestress. To visualize and classify SFs into their subtypes in live cells, we stably transduced U2OS cells with RFP-LifeAct and GFP-paxillin to label F-actin and FAs, respectively. Following severing, we tracked the retraction distance, defined as one-half the distance between the severed ends, over time (Figure 1B and Supplemental Movies S1–S3). As described in our earlier studies, the plateau retraction distance of SFs directly reflects the amount of tension or prestress borne by the fiber (Kumar *et al.*, 2006; Tanner *et al.*, 2010; Chang and Kumar, 2015; Kassianidou *et al.*, 2017a). In those studies, the plateau retraction distance was a parameter that was extracted from fitting the SF retraction traces, which typically followed negative exponential curves, to the KV equation. Assuming good agreement between the retraction trace and the fitted KV equation, the plateau retraction distance parameter should be equivalent to the measured retraction distance. In our current study, dorsal SF retractions did not follow KV behavior (Figure 1B). Thus, to facilitate comparisons between subtypes, we compared the measured retraction distance at 45 s, the time point at which SFs largely ceased to retract. Dorsal SFs retracted a shorter distance than transverse arcs ($p < 0.0001$) and ventral SFs ($p < 0.0001$) (Figure 1C), consistent with the lack of ppMLC staining along dorsal SFs. There was also a weak positive correlation between ventral SF length and retraction distance (Spearman's rank correlation coefficient $\rho = 0.46$), consistent with the idea that longer fibers contain more contractile units (Figure 1D) (Kassianidou *et al.*, 2017a). The divergent sizes of

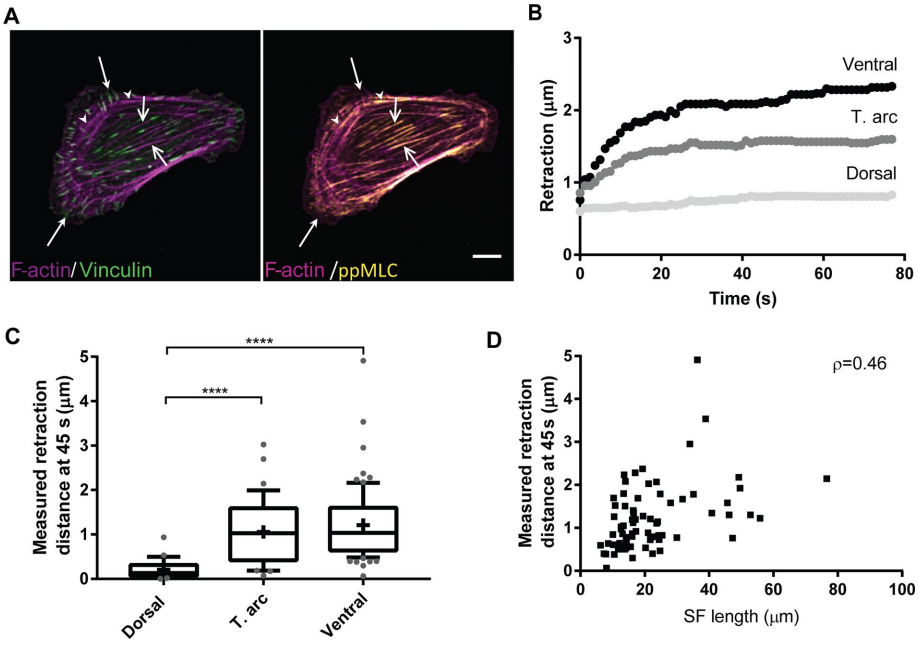

FIGURE 1: Dorsal SFs bear less prestress than transverse arcs and ventral SFs. (A) Dorsal SFs (filled arrows), transverse arcs (arrow heads), and ventral SFs (open arrows) in U2OS cells. SFs (magenta) are classified into subtypes based on their connections to vinculin clusters (green), their decoration with ppMLC (yellow), and their location in a migrating cell. Scale bar 10 μm. (B) Typical retraction traces of ablated SFs for each of the three subtypes. (C) Measured retraction distance 45 s after ablation. $N = 29, 37, 74$ dorsal SFs, transverse arcs, and ventral SFs, each from different cells, across 13–17 independent experiments. Kruskal–Wallis test, post-hoc Dunn's test, $^{****}p < 0.0001$. Cross indicates mean. Error bars show 10th and 90th percentiles. (D) Ventral SF retraction distance plotted against the SF length (Spearman's rank coefficient $\rho = 0.46$, $N = 74$ ventral SFs from C).

dorsal SFs (5–15 μm) and ventral SFs (5–80 μm) makes comparisons of length dependence challenging (Supplemental Figure S1A). Nonetheless, when we controlled for length by focusing only on fibers less than 20 μm in length, we found that ventral SFs still retracted more than dorsal SFs (Supplemental Figure S1B), with a much more pronounced length-dependent retraction.

On closer examination of dorsal SF and transverse arc retractions, we noticed that the retraction of one SF subtype was influenced by the other. When a transverse arc was severed, its retraction distance was influenced by the presence of orthogonally networked dorsal SFs (Figure 2A and Supplemental Movie S4). Connected dorsal SFs halted the retraction of one of the severed ends of the transverse arc long before the other severed end plateaued, resulting in the asymmetric retraction of the two ablated ends (Figure 2, Ai and B, traces 1 and 2). In contrast, a transverse arc that was not locally intersected by a dorsal SF retracted unhindered: both SF ends retracted at approximately the same rate and plateaued simultaneously (Figure 2, Aii and B, traces 3 and 4). When a dorsal SF was severed, the posterior fragment located closer to the cell center centripetally translocated in concert with an orthogonally associated transverse arc. The posterior segment displaced a greater distance than the anterior segment ($p < 0.0001$), suggesting that dorsal SFs are inherently noncontractile and are instead secondarily tensed by networked transverse arcs (Figure 2, C–E, and Supplemental Movie S5). These results were also supported by experiments where we severed multiple SFs in a single cell. When we simultaneously severed two adjacent dorsal SFs, the posterior and anterior severed ends of both SFs retracted similarly as in the case when one dorsal SF was severed: the posterior fragments translocated more than the anterior ones (Supplemental Figure S2A). However, when we first severed a transverse arc at two points straddling its intersection with a dorsal SF and then severed the dorsal SF, the release of tension in the transverse arc reduced both the extent and anterior/posterior asymmetry of the translocation of the dorsal SF segments (Supplemental Figure S2B and Supplemental Movie S6). Taken together, these results indicate that the dorsal SF and transverse arc networks are mechanically integrated. These findings are also consistent with a model in which myosin-containing transverse arcs exert contractile forces that are collectively transmitted to dorsal SFs, which in turn anchor to FAs and passively transmit tension from the center of the cell to anterior adhesions (Burnette *et al.*, 2014).

Genetic depletion of transverse arcs reduces prestress on ventral SFs

Given the mechanical interdependence between subtypes observed at the single-SF level, we asked what would happen to SF architecture and mechanics if we globally disrupted specific SF subtypes. To do so, we used short hairpin RNAs (shRNAs) to stably knock down (KD) palladin (90 and 140 kDa isoforms) or mDia2, which have respectively been shown to be critical in the formation of dorsal SFs and transverse arcs (Tojkander *et al.*, 2011; Gateva *et al.*, 2014). To facilitate quantification of subtype targeting, cells were cultured on fibronectin crossbow micropatterns to standardize cell shape and area (Figure 3A and Supplemental Figure S3) (Théry *et al.*, 2006). The crossbows compel the cell to adopt a polarized, migratory morphology, with dorsal SFs and transverse arcs preferentially at the curved region of the crossbow, and ventral SFs at the pointed end of the crossbow (Oakes *et al.*, 2012; Gateva *et al.*, 2014). After confirming protein depletion in our cell lines (Supplemental Figure S4A), we cultured these cells on crossbow patterns and found that palladin and mDia2 KD respectively and selectively reduced dorsal SF and transverse arc density relative to both naïve cells (palladin KD dorsal SF reduction: $p < 0.05$; mDia2 KD transverse arc reduction: $p < 0.05$) and control cells transfected with a nontargeting (NT) shRNA sequence (palladin KD dorsal SF reduction: $p < 0.001$; mDia2 KD transverse arc reduction: $p < 0.05$) (Supplemental Figure S4, B and C). On unpatterned matrices, both the mDia2 KD/transverse arc-depleted and palladin KD/dorsal SF-depleted cells displayed morphological differences (Supplemental Figure S4D). Specifically, mDia2 KD/transverse arc-depleted cells often adopted irregular shapes with multiple lamella-like projections that lacked clearly defined transverse arcs. Palladin KD/dorsal SF-depleted cells were often rounded and had numerous small, punctate adhesions along the protrusive ends, consistent with an inability of the adhesions to mature (Oakes *et al.*, 2012; Gateva *et al.*, 2014).

We returned to crossbow-patterned substrates to quantify the effects of dorsal SF and transverse arc depletion on the mechanics of remaining SFs by laser nanosurgery. We began by repeating our sequential severing experiments in patterned naïve cells, which

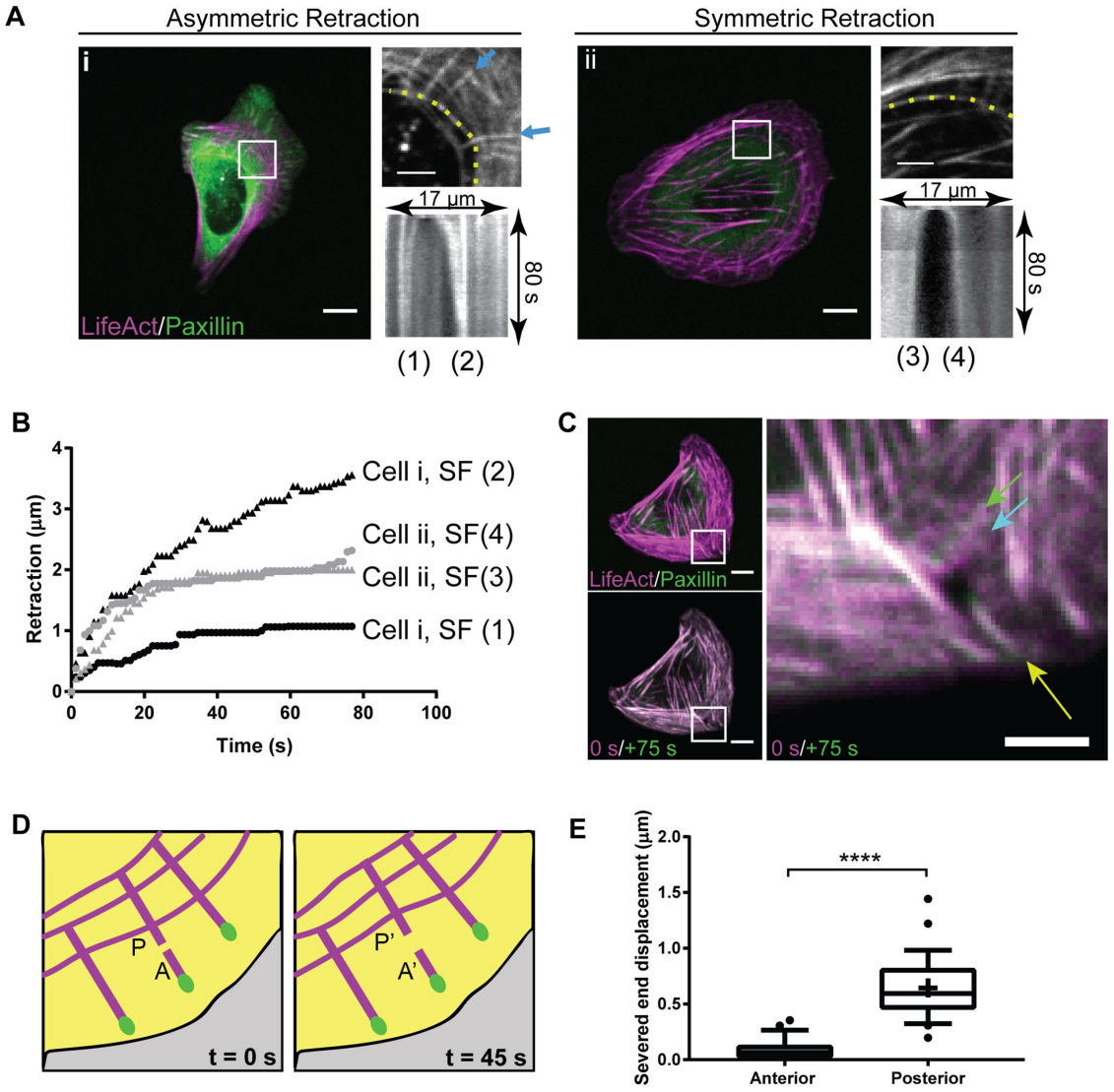

FIGURE 2: Transverse arcs are mechanically coupled to dorsal SFs. (A) Panel i, asymmetric retraction of severed transverse arc ends, or panel ii, symmetric retraction of severed transverse arc ends due to the presence or absence of dorsal SFs in the immediate vicinity of the ablation site. Inset and kymograph show the region of interest and the retraction of the transverse arc. Dashed yellow lines indicate the severed transverse arc, and blue arrows point to networked dorsal SFs. (B) Retraction traces of the severed transverse arc ends shown in A. Black traces (1) and (2) correspond to panel i. Gray traces (3) and (4) correspond to panel ii. (C) After severing, the posterior fragment of a dorsal SF translocates with a connected transverse arc, whereas the anterior severed end translocates a short distance. Top left panel shows cell before the dorsal SF (yellow arrow) is ablated. Bottom left shows a before/after overlay. Inset shows the region of interest. The cyan and green arrows indicate the location of the transverse arc before and after ablation of the dorsal SF, respectively. (D) The translocation of each severed dorsal SF end is tracked. A, anterior end closer to the leading edge of the cell; P, posterior end closer to the cell center. (E) Measured displacement of anterior and posterior severed dorsal SFs ends 45 s after severing. Wilcoxon matched-pairs rank test, ****$p < 0.0001$, $N = 29$ dorsal SFs, each from different cells across 13 independent experiments. Cross indicates mean. Error bars show 10th and 90th percentiles. Scale bar: 10 µm for main panel, 5 µm for insets.

revealed similar interdependences between dorsal SFs and transverse arcs (Supplemental Figure S5 and Supplemental Movie S7). Next, we considered our palladin and mDia2 KD cells; we focused on measuring retraction profiles of ventral SFs, since this was the most prominent subtype in our cell lines and because we did not observe changes in transverse arc and dorsal SF retraction on depletion of the other subtypes (Figure 3A, Supplemental Movie S8, and Supplemental Figure S6). To quantitatively compare retraction across cell lines, we fitted the retraction kinetics of ventral SFs to a KV model (Kumar *et al.*, 2006; Tanner *et al.*, 2010) (Figure 3B). As discussed earlier, this model enables extraction of two parameters: L_o, the plateau retraction distance of the severed SF and a measure of stored elasticity, and τ, the exponential time constant of retraction, which represents the ratio of SF viscosity to elasticity. A third parameter, D_a, is the fitted length of the SF destroyed during the ablation. By comparing L_o values, we found that ventral SFs in the mDia2 KD/transverse arc-depleted cells had lower prestresses than in palladin KD/dorsal SF-depleted ($p < 0.05$), NT ($p < 0.05$), and naïve ($p < 0.05$) cells. Depletion of either protein/SF subtype did not significantly influence τ values (Figure 3C). Consistent with this reduction in

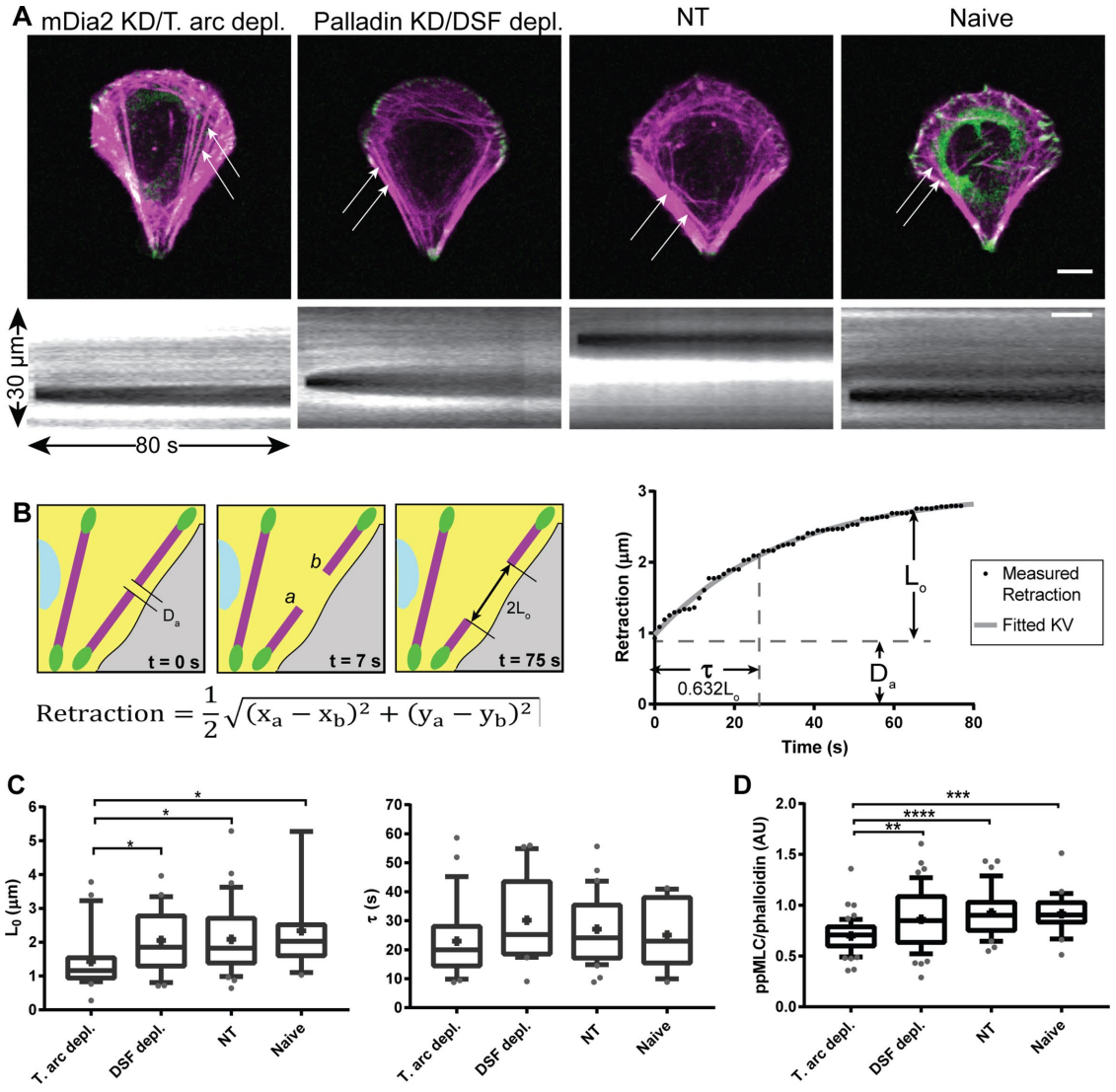

FIGURE 3: Ventral SFs in cells with depleted transverse arcs have altered retraction kinetics. (A) Top, representative images of mDia2 KD/transverse arc-depleted, palladin KD/dorsal SF-depleted, NT control, or naïve control cells on crossbow micropatterns. Bottom, kymographs of ablated ventral SF indicated by the white arrow in the top panel showing retraction. Scale bar 10 µm. (B) Schematic of SF retraction measurement and analysis. The retraction of ventral SFs is measured by taking one-half of the distance between the severed ends. The resulting retraction vs. time profile can be fitted to the KV model for viscoelastic materials, with characteristic parameters L_o (elastic prestress), τ (viscoelastic time constant), and D_a (length of SF destroyed during ablation). (C) Fitted KV parameters for ventral SFs in each of the cell lines. (D) Analysis of ppMLC intensity in ventral SFs, normalized to phalloidin. mDia2 KD/transverse arc-depleted cells contain less ppMLC. $N = 24, 21, 34, 13$ SFs from different mDia2 KD/transverse arc-depleted, palladin KD/dorsal SF-depleted, NT, or naive cells across seven to nine independent experiments for C. $N = 56, 48, 37, 23$ SFs from different mDia2 KD/transverse arc-depleted, palladin KD/dorsal SF-depleted, NT, or naive cells across two independent experiments for D. *$p < 0.05$, **$p < 0.01$, ***$p < 0.001$, ****$p < 0.0001$, Kruskal–Wallis test, post-hoc Dunn's test. Cross indicates mean. Bars extend to 10th and 90th percentiles.

prestress, ventral SFs in the mDia2 KD/transverse arc-depleted cells also had lower levels of ppMLC staining (vs. palladin KD/dorsal SF-depleted: $p < 0.01$; vs. NT: $p < 0.0001$; vs. naïve: $p < 0.0001$) (Figure 3D). Together, the altered retraction kinetics and ppMLC localization indicate that ventral SFs in transverse arc-depleted cells are less tensed due to lower levels of myosin activity.

Ventral SFs commonly fail to plateau in palladin KD/dorsal SF-depleted cells

During our analysis of ventral SF retraction, we noticed that there was a subset of fibers in the SF-depleted and control cells with fitted τ values that exceeded 60 s. These extended retraction events were excluded from the analysis of KV parameters (Figure 3), as the large τ values suggested that the fiber did not fully plateau in the 77 s tracking window (Supplemental Figure S7 and Supplemental Movie S9). In the case of the palladin KD/dorsal SF-depleted cells, these fibers retracted with kinetics that were more linear than exponential. We verified that these nonplateauing retractions were not due to SF depolymerization; in separate experiments, we photobleached fiducial markers along the length of the SF and observed that these marks translocated in coordination with the severed ends following incision of the fiber (Supplemental Figure S8) (Kumar *et al.*, 2006).

In previous work, we had shown that internal and external cross-linking can serve as a brake that limits SF retraction (Chang and Kumar, 2015; Kassianidou *et al.*, 2017a). Thus, we initially hypothesized that the atypical SF retractions might be due to altered cross-linker morphology along SFs. Internal cross-linkers within an SF would include the components of noncontractile dense bodies, such as α-actinin and palladin, which stiffen the SF and limit retraction (Chang and Kumar, 2015). External cross-linkers are structures outside of the ablated SF that might influence retraction of the severed ends, such as other networked SFs (Kassianidou *et al.*, 2017a) and nascent cell-matrix adhesions (Colombelli et al., 2009). Given that palladin is an actin cross-linker and a key component of dense bodies (Dixon *et al.*, 2008; Grooman *et al.*, 2012; Azatov *et al.*, 2016), suppression of palladin might be expected to globally destabilize SF internal cross-linking. To assess dense body architecture, we stained for α-actinin-1, a cross-linking protein that interacts and colocalizes with palladin in dense bodies (Rönty *et al.*, 2004). Surprisingly, structured illumination microscopy (SIM) revealed that the cross-linking morphology was similar along the center of ventral SFs across both the palladin KD/dorsal SF-depleted cells and the NT cells, with α-actinin-1 localizing to SFs in regularly spaced puncta (Figure 4A). Therefore, we concluded that palladin suppression does not broadly disrupt internal SF cross-linking, making altered cross-linking at the center of the SF an unlikely cause of nonplateauing retractions.

We next hypothesized that the nonplateauing ventral SF retraction might be related to the absence of dorsal SFs. We arrived at this idea because ventral SFs can form through at least two routes: the fusion of two dorsal SFs flanking transverse arcs during retrograde SF flow or from the de novo annealing of short actomyosin fragments (Machesky and Hall, 1997; Hotulainen and Lappalainen, 2006; Vallenius, 2013; Tojkander *et al.*, 2015). In the former case, progenitor transverse arcs would be expected to confer elastic prestress to their ventral SF progeny through the contribution of myosin motors, which dorsal fibers lack. Conversely, dorsal SFs, which are rich in cross-linkers (Oakes *et al.*, 2012; Burnette *et al.*, 2014; Gateva *et al.*, 2014) and passively transmit tension from transverse arcs to FAs, might facilitate SF braking during retraction. As we have shown, ventral SFs in mDia2 KD/transverse arc depleted cells are under lower prestress, and some ventral SFs in palladin KD/dorsal SF-depleted cells have altered retraction profiles. Consistent with this idea, α-actinin-1 continuously decorates dorsal SFs rather than assembling into the sarcomeric puncta seen in transverse arcs and ventral SFs (Figure 4A). Furthermore, the termini of ventral SFs (corresponding to the location of FAs) in palladin KD/dorsal SF-depleted cells have shorter regions of continuous α-actinin staining than ventral SF termini in NT cells (Figure 4, B–E). Thus, the linear retraction kinetics of ventral SFs in the palladin KD/dorsal SF-depleted cells could be a consequence of reduced SF braking. In the de novo ventral SF formation pathway, actomyosin bundles are annealed together without the participation of cross-linker–rich dorsal SFs, such that the resulting SFs would also be expected to have atypical retractions.

Cell shape and SF architecture can be controlled by patterning thin-width microlines

If the above hypothesis is true, then compelling cells to form ventral SFs through de novo assembly (rather than dorsal SF/transverse arc fusion) should strongly reduce braking during retraction and favor linear or atypical SF retractions. To achieve this regime, we constrained cells to patterned fibronectin microlines of widths ranging from 2 to 50 µm (Figure 5A). The thinner microlines (e.g., 2-µm-wide) laterally constrain cell spreading to an extent that precludes assembly of canonical lamella, with a corresponding absence of dorsal SFs and transverse arcs (Supplemental Figure S9 and Supplemental Movie S10). On such matrices, the SF network would be dominated by ventral SFs, which would necessarily have to arise from de novo actomyosin assembly rather than dorsal SF/transverse arc fusion. Indeed, when cultured on 2-µm microlines, all cell lines adopted a spindle-like morphology with two long ventral SFs running the length of the cell along the outer edge of the pattern (Figure 5B). As expected, wider microlines were increasingly permissive to lamella formation and cells began to resemble those on unpatterned substrates. NT and naïve cells on 10-µm-wide lines displayed short dorsal SFs near one end of the cell and, in some cases, short and slightly curved SFs reminiscent of transverse arcs. On the 50-µm microlines, the NT and naïve cells were able to form all three SF subtypes. mDia2 KD/transverse arc-depleted and palladin KD/dorsal SF-depleted cells similarly began to take on their respective morphologies on unpatterned matrices with increasing microline width.

Atypical/non-KV ventral SF retractions decrease in frequency with increasing microline width for all cells with the exception of palladin KD/dorsal SF-depleted cells

When we ablated ventral SFs in cells on the 2-, 10-, and 50-µm microlines, we found that the 77 s imaging window that we used previously was often insufficient to fully capture the retraction profile of the severed SF ends, with many SFs failing to reach a plateau within that time (Figure 6A and Supplemental Movie S11). We therefore extended the imaging window to 155 s and noticed that the retraction profiles fell within three categories: 1) negative exponential that fit a KV retraction (typical for ventral SFs in NT and naïve cells), 2) linear, or 3) retraction in two, or occasionally more, stages, with some permutation of linear and exponential retractions (Figure 6B, Supplemental Figure S10, and Supplemental Movie S12). There were instances of atypical/non-KV retractions in all cell lines on the 2-µm microlines (Figure 6, C and D, and Supplemental Figure S10), which, as described above, only permit assembly of ventral SFs. The proportion of atypical/non-KV retractions (retraction profiles 2 and 3) encompassed more than 50% of the ablated SFs in each cell line and was not significantly different between cell lines ($p = 0.63$) (Figure 6E, left). Since ventral SFs in all cells on the 2-µm microlines are qualitatively similar in terms of SF architecture and prestress, we conclude that dorsal SFs and transverse arcs do not contribute appreciably to overall SF network assembly in these confined settings.

On wider 10- and 50-µm microlines, NT and naïve cells can increasingly form dorsal SFs and transverse arcs and, subsequently, a population of ventral SFs from these precursor fibers. Correspondingly, as the microline width increases, the proportion of ventral SFs displaying KV retractions in control cells also increases and consists of up to 88% of the ablated fibers in cells on the 50-µm microlines. We observed a similar trend in the mDia2 KD/transverse arc-depleted cells; however, only 60% of retraction events follow KV kinetics in palladin KD/dorsal SF-depleted cells on 50-µm microlines (Figure 6E, middle and right), which is significantly lower than in all other cell lines ($p < 0.01$). These results suggest that dorsal SFs may influence ventral SF retraction by braking the retraction of SFs. Without this brake, SFs exhibit atypical, extended retraction profiles.

DISCUSSION

SFs in migrating cells are canonically categorized into three subtypes based on their location, composition, and anchorage to FAs.

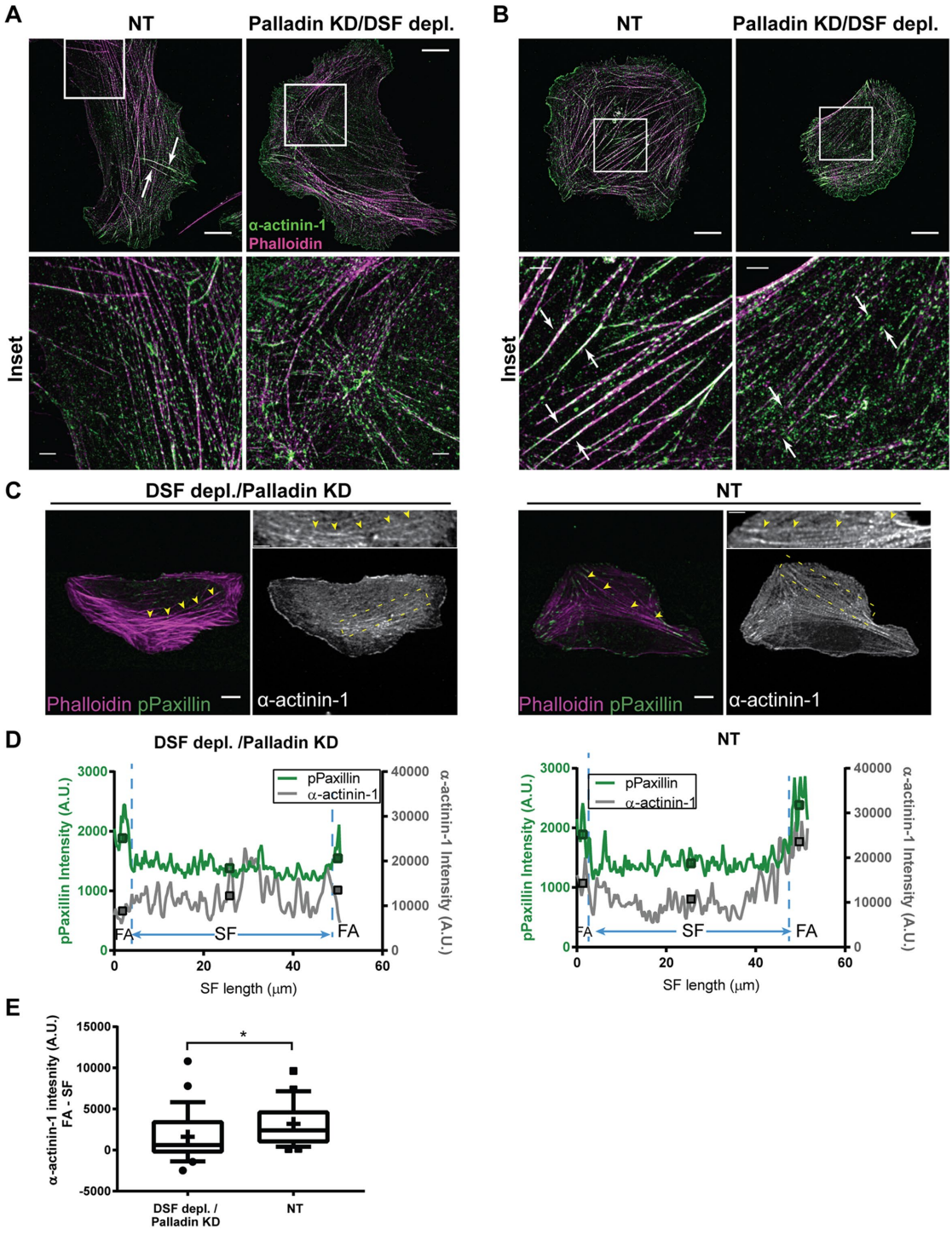

FIGURE 4: Palladin KD-mediated depletion of dorsal SFs does not grossly destabilize ventral SF dense body organization at the SF center. (A) Periodic clusters of α-actinin-1 (green) cross-linkers along transverse arcs and ventral SFs in SIM images of NT or palladin KD/dorsal SF-depleted cells. SFs are stained using phalloidin (magenta). Arrows point to dorsal SFs, which have continuous α-actinin-1 staining. (B) α-actinin-1 enrichment at the ends (white arrows) of ventral SFs in NT cells. These regions are not present in palladin KD/dorsal SF-depleted cells. For A and B, the bottom row depicts high-magnification images of the insets (white boxes). Scale bars: 10 μm (top row), 2 μm (bottom row). (C) Representative confocal images of palladin KD and NT cells stained for paxillin (green), F-actin (magenta), and α-actinin-1 (gray). Box indicates region of interest containing a ventral SF (yellow arrowheads) that is measured. Scale bar: 10 μm, inset: 5 μm. (D) Line scans of the indicated ventral SFs in the paxillin (green) and α-actinin channels (gray). Vertical dashed blue lines delineate the FA regions, as determined by paxillin fluorescence, from the rest of the SF. Squares indicate mean fluorescence intensity of the indicated region. Line scans were used to determine the difference in average α-actinin-1 fluorescence intensity at the FA ends of SF and the center of the SF. (E) Difference in the average α-actinin-1 intensity at the FA ends and at the center of the SF for 28 palladin KD/DSF-depleted or 24 NT cells (one to three SFs measured per cell) from three independent experiments. *$p < 0.05$, Wilcoxon rank sum test.

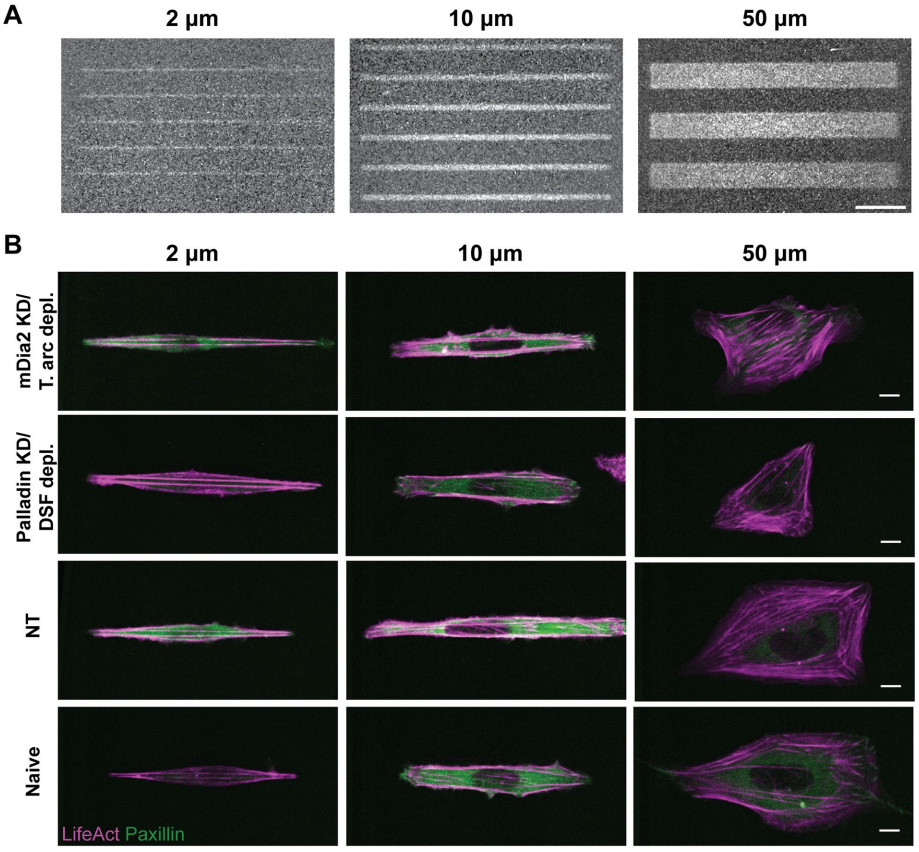

FIGURE 5: Ventral SFs on microline-patterned cells. (A) Patterning of fibronectin microlines onto glass coverslips, visualized with fluorescently labeled fibronectin. Scale bar: 100 µm. (B) Representative LifeAct (magenta)/paxillin (green) images of cells patterned on 2-, 10-, or 50-µm microlines. Scale bar: 10 µm.

By combining single-SF laser nanosurgery, subtype-specific depletion, and micropatterning, we have directly demonstrated that each subtype bears unique, nonoverlapping mechanical properties and structural roles. These differences arise in turn from both intrinsic variations in composition across the subtypes and extrinsic variations in connectivity to other SFs and presumably other cytoskeletal elements. Specifically, our work reveals that dorsal SFs bear little intrinsic prestress and instead are externally tensed by mechanically coupled contractile transverse arcs. Furthermore, ventral SFs, which may form from the fusion of dorsal SFs and transverse arcs, depend on the integrity of both of these progenitor SF pools, as depletion of either subtype influences ventral SF retraction kinetics (Figure 7).

Our results represent the first direct, subtype-specific measurements of SF mechanical function, and, as such, complement and directly test predictions of more indirect, cell-scale analyses of SF networks. In particular, a recently proposed model assigns dorsal SFs and transverse arcs different roles in shaping the flattened lamella of migrating cells (Burnette *et al.*, 2014). Specifically, transverse arcs are postulated to contract, thus pulling on rigid dorsal SFs, which lever against the ECM through FAs and produce a flattened lamella. This elegant model was deduced in part from loss-of-function studies in which transverse arcs were dissipated through the use of contractility inhibitors (e.g., blebbistatin, Y-27632) or myosin IIA KD (Burnette *et al.*, 2014). The influence of both interventions would be expected to extend beyond transverse arcs, as evidenced by the finding that contractility inhibition and myosin IIA KD also reduced the population of ventral SFs (Burnette *et al.*, 2014). As another example, model-based traction force microscopy has been used to deduce tension borne by individual SFs by reconciling traction force maps against SF and FA distributions through an elastic cable network model (Soiné *et al.*, 2015). However, this approach is computationally intensive, depends on a specific mechanical model, and requires high-resolution imaging and traction force measurements. Our study addresses many of these gaps by applying laser nanosurgery to conduct direct loss-of-function studies on single SFs. These measurements enable us to disrupt single SFs in an isolated manner and invoke simple KV models of viscoelasticity to infer prestress. In doing so, our results support and integrate predictions of both measurements into a unified picture of SF network mechanics: dorsal SFs are intrinsically noncontractile and are tensed by associated transverse arcs, which are reciprocally constrained by their connections to dorsal SFs. Additionally, ventral SFs bear the greatest prestress of any subtype, consistent with their role in detaching mature adhesions at the trailing edge of the cell (Vicente-Manzanares *et al.*, 2008, 2009, 2011).

Our results also offer new insights into how the mechanical properties of ventral SFs relate to their mechanism of formation. Ventral SFs have been observed to form from the fusion of dorsal SFs and transverse arcs during retrograde flow (Cramer *et al.*, 1997; Hotulainen and Lappalainen, 2006; Tojkander *et al.*, 2015). However, it has been unclear how the structure and mechanics of progenitor SFs might affect the properties of the resulting progeny ventral SF. By selectively depleting dorsal SFs or transverse arcs and severing the remaining ventral SFs, we have gathered support for a model in which ventral SF retraction is driven by myosin derived from progenitor transverse arcs and braked by cross-linkers derived from dorsal SFs (Figure 7). Specifically, contractile transverse arcs contribute NMII to newly formed ventral SFs during retrograde flow, with increased contractile loads leading to the incorporation of more NMII units to the fiber. Noncontractile dorsal SFs contribute additional braking elements (i.e., SF cross-linkers), which continuously decorate, rather than sarcomerically organize, within dorsal SFs. We speculate that the dorsal SFs positioned at either end of the protoventral SF act as either internal braking regions that stop the progressive collapse of sarcomeric units along an SF when severed or as tethering points to matrix adhesions or cytoskeletal elements.

Knockdown of mDia2 or palladin enabled us to examine the contributions of transverse arcs and dorsal SF subtypes to ventral SF mechanics. Selectively depleting transverse arcs by knocking down mDia2 results in weakly contractile ventral SFs, which can be attributed to the progenitor fibers lacking a contractile element. Some NMII from the cytoplasmic pool may be incorporated along the length of this ventral SF; but overall, the fiber is under less prestress. On the other hand, reduction of dorsal SFs via palladin depletion results in ventral SFs with impaired braking during retraction.

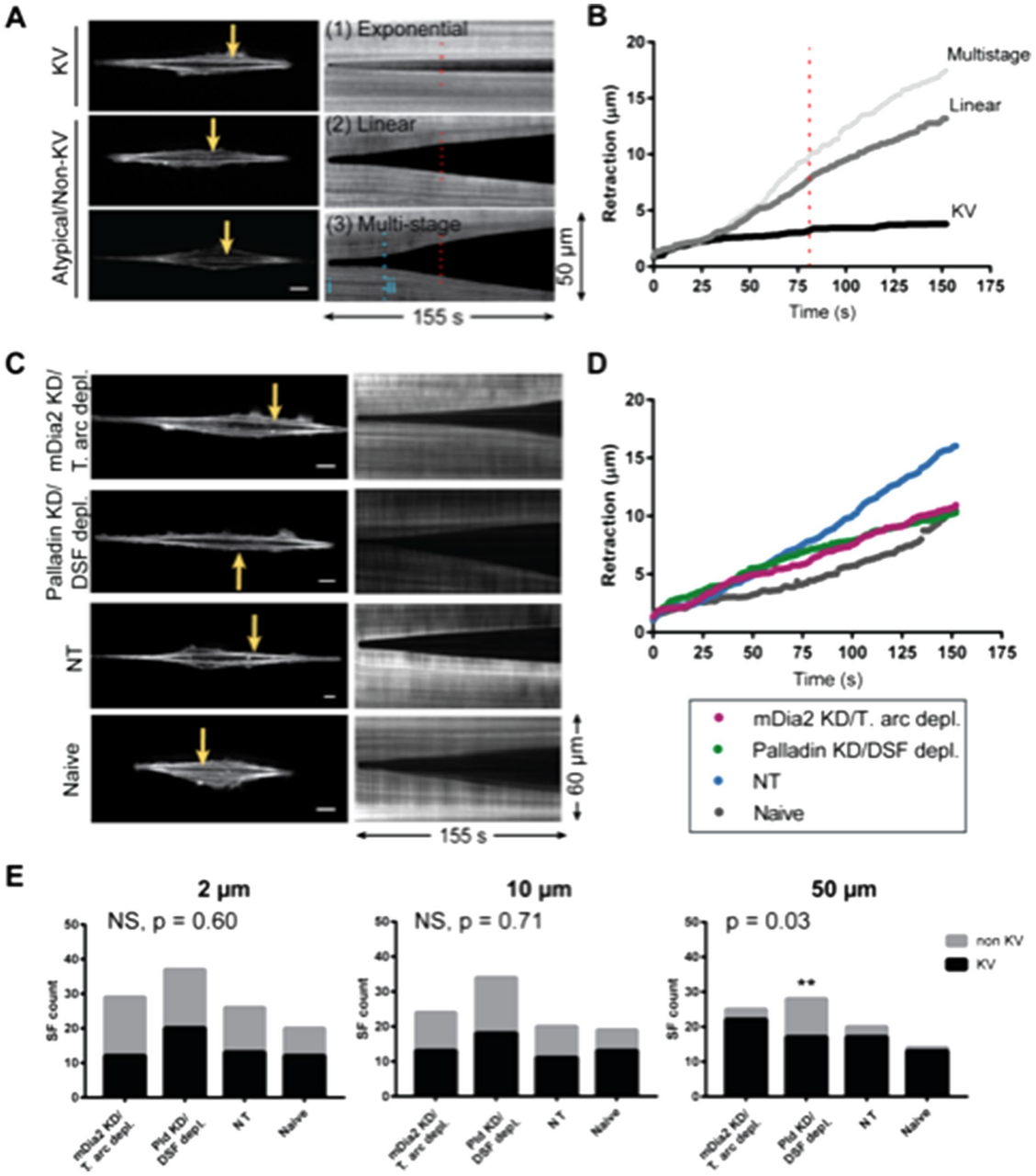

FIGURE 6: Microline-constrained cells exhibit atypical retraction profiles. (A) Typical kymographs and corresponding retraction traces of ablated SFs (yellow arrows) in NT cells on 2-μm microlines. Three categories of retraction profiles, 1) exponential (KV), 2) linear (non-KV), or 3) multistage (non-KV, stages are demarcated by dashed blue line), are observed. The red dashed line is the halfway point or 77 s. (B) Retraction traces of the kymographs from A. (C) Example non-KV retractions of severed ventral SFs (yellow arrow) on 2-μm microlines. Kymographs show the retraction of the indicated fiber. Scale bar: 10 μm. (D) Retraction traces of the kymographs in C. (E) Distribution of retraction profiles for ventral SFs in each of the cells on 2-, 10-, or 50-μm microlines; 2-μm pattern: $N = 29, 37, 26, 20$ ventral SFs; 10-μm pattern: $N = 24, 34, 20, 19$ ventral SFs; 50-μm pattern: $N = 24, 28, 20, 14$ ventral SFs, each from different mDia2 KD/transverse arc-depleted, palladin KD/dorsal SF-depleted, NT, and naïve cells, respectively. Cells are from five to nine independent experiments. The p values are from a chi-square test for cells on 2- or 10-μm microlines or from the Fisher's Exact test for cells on 50-μm microlines. $^{**}p < 0.01$: post-hoc comparison between palladin KD/DSF depleted cells and other cell lines. NS, not significant.

Specifically, dorsal SFs contribute cross-linkers that slow and eventually halt retraction as the tension released by the collapsing sarcomeres is eventually balanced by the load placed on the cross-linkers. In support of the braking role of cross-linkers, SIM images of the NT controls showed an enrichment in α-actinin-1 at the ends of ventral SFs where FAs are expected to be. These enriched regions were largely reduced in the palladin KD/dorsal SF-depleted cells (Figure 4, B–E). Similarly, ventral SFs that form de novo from the annealing of short actomyosin fragments (i.e., independent of dorsal SFs and transverse arcs, as in cells on 2-μm-wide microlines) also have

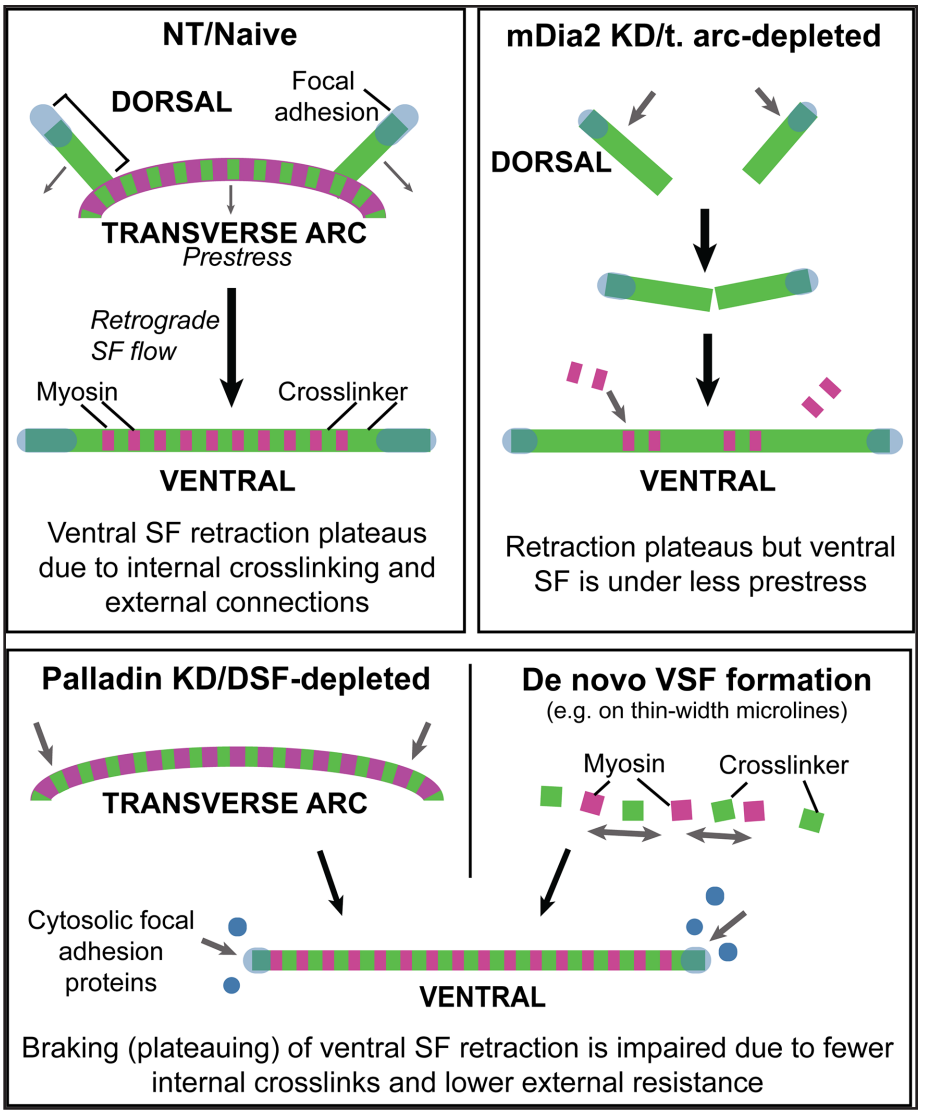

FIGURE 7: Model of ventral SF viscoelastic properties. Ventral SFs may form from the fusion of transverse arcs and dorsal SFs (e.g., in NT/naïve cells). Precursor transverse arcs contain NMII, which contributes prestress, and precursor dorsal SFs contribute braking elements that lead to the plateauing of the subsequently formed ventral SF. Ventral SFs in transverse arc-depleted cells are under less prestress because they are deficient in NMII introduced by transverse arcs. Ventral SFs that form in dorsal SF-depleted cells or de novo lack the cross-linker regions that contribute to braking SF retraction.

impaired braking as they are presumably not enriched in cross-linkers at the ends. The cross-linkers at the ends and in dense bodies along the center length of the fiber may also act as brakes by physically inducing nascent adhesion formation as the cut ends of the fiber slide along the basal membrane, as others have proposed (Colombelli et al., 2009). Our images did not reveal the presence of canonical ECM adhesions or connections to other actin-based structures in these regions. However, both α-actinin and palladin cross-linkers are known to bind to FA proteins (Parast and Otey, 2000; Otey and Carpen, 2004; Sjöblom *et al.*, 2008). Thus, dorsal SF depletion via palladin KD, or a reduction in cross-linker density anywhere along the length of the fiber, could reduce restoring forces and impair the arrest of SF retraction. Our findings and model are consistent with past studies of single SF mechanics, including our own past work showing that kinase-specific induction of myosin activation within an SF increases its prestress without dramatically changing the viscoelastic time constant (Kassianidou *et al.*, 2017b). Similarly, our current study reveals that depletion of transverse arcs reduces the levels of active myosin in ventral SFs, concurrently lowering prestress without significantly affecting the viscoelastic time constant. Nevertheless, we fully acknowledge that myosin, internal cross-links, and external connections are each likely to contribute to SF viscoelastic properties in complex ways and that additional studies are needed to directly and critically test specific aspects of our model.

While palladin and mDia2 KD have been previously used to deplete SF subtypes (Tojkander *et al.*, 2011; Gateva *et al.*, 2014), we do note that a limitation of this approach is the likelihood of collateral effects on cell function, including FA dynamics and microtubule stability (Gupton *et al.*, 2007; Azatov *et al.*, 2016). We thus turned to the use of one-dimensional ECM patterns as an independent way of manipulating SF subtypes. By varying the width of ECM patterns, we were able to control the formation of SF subtypes and examine the resulting effect on SF retraction behavior. On the narrowest (2-μm) microlines, we observed that a large proportion of ventral fibers in all of our cell lines had atypical/nonplateauing retractions, with this proportion decreasing for all cells, except for the palladin KD/dorsal SF-depleted cells, on the 50-μm microlines. The 2-μm microlines led to cells with mutually similar shapes, and thus similar SF architectures and SF retraction profiles, since ventral SFs are forced to form from the de novo pathway. However, the abundance of atypical retractions on the 2-μm microlines could also be accounted for by the polarization of traction forces, which would be expected to increase the tension borne by a single fiber. The vast majority of the SFs in these constrained cells are oriented parallel to the pattern, meaning that there are few connections to other SFs that could absorb the released tension. Migration and traction force studies have shown that thin microlines readily polarize the cell and concentrate forces at the front and back of the cell (Doyle *et al.*, 2009; Leal-Egaña *et al.*, 2017). Finally, the SFs that were ablated tended to be long (median lengths are ~60 μm, though some can exceed 100 μm), which may mean that a longer time window is needed to fully capture the full retraction profile of the SF, as we have shown that the viscoelastic time constant of the SF increases with length (Kassianidou *et al.*, 2017a).

Our work demonstrates that the three canonical SF subtypes exhibit distinct structural roles and interconnect to form a physically integrated network. Because of this integration, compromise of one subpopulation influences the other, a conclusion supported by both our single-SF nanosurgery and subtype-specific knockdown studies.

An important open question is how these relationships manifest themselves in more complex ECMs, including three-dimensional fibrous matrices representative of connective tissue. One-dimensional microlines have been shown to capture defining features of three-dimensional motility (Doyle *et al.*, 2009), raising the intriguing possibility that the SF mechanics we observe on microlines may offer predictive insights into three-dimensional matrices. Future studies exploring the mechanics of single SFs in these complex matrices should offer valuable insight into how individual SFs tense the cytoskeleton and ultimately establish shape homeostasis and directional migration.

MATERIALS AND METHODS

Cell culture and knockdowns

U2OS cells (ATCC HBT-96) were maintained in DMEM (Life Technologies) supplemented with 10% fetal bovine serum (FBS) (JR Scientific), 1% nonessential amino acids (Life Technologies), and 1% penicillin/streptomycin (Life Technologies). Cells were tested for mycoplasma every 3 mo and authenticated via short tandem repeat profiling.

Cloning and cell line generation

To create knockdown cells, we used shRNA constructs targeting all nine isoforms of palladin (5′-AATCACTACACCATTCAAAGA-3′) or mDia2 (5′-AAGCAGAGCTACAAGCTTTTA-3′). A nontargeting sequence (NT: 5′-GCTTCTAGCCAGTTACGTACA-3′) was also included as a control. Each oligonucleotide was inserted into the pLKO.1-TRC cloning vector (Addgene plasmid #10878) using *Age*I and *Eco*RI (Moffat *et al.*, 2006) (verified by sequencing). pYFP-paxillin (Addgene plasmid #50543) was cloned into the pLVX-AcGFP vector using *Xho*I and *Eco*RI. RFP-LifeAct was cloned into the pFUG vector as described previously (Lee *et al.*, 2016).

Lentiviral particles were packaged in HEK 293T cells. shRNA viral particles were used to transduce U2OS cells at a multiplicity of infection (MOI) of 1. Cells were selected using 2 μg/ml puromycin (Clontech). Following confirmation of KD via Western blot and immunofluorescence characterization, cells were subsequently transfected with pFUG-RFP LifeAct (MOI 3) and pLVX-AcGFP-Paxillin (MOI 0.5) particles and sorted with a BD Bioscience Influx Flow Cytometer Sorter. U2OS cells are reported to express five palladin isoforms (Gateva *et al.*, 2014), although we were able to verify the KD of only the 140 and 90 kDa isoforms.

Micropatterning

Micropatterns were made as described elsewhere (Théry *et al.*, 2006; Carpi *et al.*, 2011; Tseng *et al.*, 2011; Kassianidou *et al.*, 2017a). Briefly, plasma-treated coverslips were coated with 10 μg/ml poly-L-lysine grafted to polyethylene glycol (PLL-g-PEG; SuSoS) in 10 mM HEPES, pH 7.4, for 1 h at room temperature before being illuminated under 180 nm UV (Jelight) light for 15 min though a quartz-chrome mask bearing the micropattern features (FineLine Imaging) designed using AutoCAD (Autodesk). Coverslips were then incubated with 20 μg/ml fibronectin (EMD Millipore) in 50 mM HEPES overnight at 4°C and washed with phosphate-buffered saline (PBS) prior to cell seeding. To visualize micropatterns, AlexaFluor-647-conjugated fibronectin, at a final concentration of 5 μg/ml was added to the coverslip. To conjugate AlexaFluor-647 to fibronectin, fibronectin stock solution (1 mg/ml; EMD Millipore) was mixed with AlexaFluor-647 NHS ester (reconstituted at 0.025 mg/ml in dimethyl sulfoxide (DMSO) (Sigma), Life Technologies) in carbonate buffer, pH 9.3, overnight at 4°C. The solution was then passed through a NAP-5 column (GE Healthcare) to separate the conjugated fibronectin.

Western blot

Cells were lysed in radioimmunoprecipitation assay (RIPA) buffer (Sigma) with phosphatase and protease inhibitors (EMD Millipore) and heated to 70°C. Samples were run on a 4–12% Bis–Tris gel (Life Technologies) and transferred to a polyvinylidene fluoride (PVDF) membrane (Life Technologies). The following primary antibodies were used: rabbit anti-palladin (1:1000; Sigma), rabbit anti-mDia2 (1:750; ProteinTech), mouse anti-GAPDH (1:10,000, Sigma). The following secondary antibodies were used: goat anti-mouse horseradish peroxidase (HRP)-conjugate, goat anti-rabbit HRP-conjugate (both from Life Technologies). HRP-conjugated bands were imaged using enhanced chemiluminescence reagent (ECL, Thermo Fisher).

Immunostaining

Cells were fixed in 4% (vol/vol) paraformaldehyde (Alfa-Aeser) for 10 min at room temperature and rinsed with PBS. Cells were permeabilized in PBS containing 5% (vol/vol) goat serum (Thermo Fisher) and 0.5% (vol/vol) Triton-X (EMD Millipore) for 10 min. Cells were blocked in PBS containing 5% (vol/vol) goat serum for 1–16 h at room temperature or at 4°C, respectively. Coverslips were incubated with primary antibodies for 2–3 h at room temperature, rinsed with 1% (vol/vol) goat serum in PBS, and then incubated with secondary antibodies and phalloidin (Life Technologies) for 1–2 h at room temperature in the dark. Cells were rinsed in PBS and mounted using Fluoromount-G (Southern Biotech).

The following primary antibodies were used for immunostaining: mouse anti-vinculin hVin-1 (1:200; Sigma), rabbit anti-diphosphorylated myosin light chain Thr18/Ser19 (1:200; Cell Signaling Technologies), mouse anti-α-actinin-1 Clone BM 75.2 (1:200; Thermo Fisher), rabbit anti-phosphorylated paxillin Tyr188 (1:200; Cell Signaling Technologies). The following secondary antibodies were used: AlexaFluor 488 anti-rabbit (1:400), AlexaFluor 647 anti-mouse (1:400), phalloidin-AlexaFluor 546 (1:200), all from Life Technologies.

Imaging

Unpatterned or micropatterned coverslips were coated with 20 μg/ml fibronectin in 10 mM HEPES, pH 8.5, overnight at 4°C and rinsed extensively. U2OS cells were seeded at 3000 cells/cm^2 and allowed to adhere for 4–6 h. Prior to imaging, the medium was changed to phenol red-free DMEM (Life Technologies) supplemented with 10% FBS, 1% nonessential amino acids, 1% penicillin/streptomycin, and 25 mM HEPES (imaging media).

Confocal imaging. For laser ablation and fixed cell studies, an upright Olympus BX51WI microscope (Olympus Corporation) equipped with Swept Field Confocal Technology (Bruker) and a Ti:Sapphire 2-photon Chameleon Ultra II laser (Coherent) was used. The 2-photon laser was set to 770 nm and single SF ablation was performed using three 20-ms exposures. Cells were imaged again at least 20 min after ablation to verify viability and membrane integrity. Live cell imaging was performed using an Olympus LUMPlanFL N 60×/1.0 water dipping objective or an Olympus UPlan FL N 10×/0.3 air objective. Cells were kept at 37°C using a stage-top sample heater (Warner Instruments). Fixed cell imaging was performed using an Olympus UPlanSApo 60×/1.35 oil immersion objective. Images were captured using an electron-multiplying charge-coupled device (EM-CCD) camera (Photometrics). The following emission filters were used: Quad FF-01-446/523/600/677-25 (Semrock) and 525/50 ET525/50 (Chroma). PrairieView Software (v. 5.3 U3, Bruker) was used to acquire images.

Epifluorescence imaging. For live cell spreading studies, a Nikon Ti-E inverted microscope was used with a 40×/0.75 Ph2 dark low low (DLL) objective and a xenon arc lamp (Lambda LS; Sutter Instrument). The microscope is equipped with a motorized, programmable stage (Applied Scientific Instrumentation) and a stage-top sample heater to maintain optimal humidity, CO_2 levels, and temperature (In Vivo Scientific). Images were acquired using a cooled CCD camera (Photometrics Coolsnap HQ2) and Nikon Elements Software.

Structured illumination microscopy imaging. Samples were fixed, stained, and mounted as described above. Samples were imaged using a Zeiss Elyra PS.1 structured illumination microscope (Zeiss) and a 63×/1.4 oil DIC M27 objective (Zeiss).

Image analysis

For visualization purposes, contrast was adjusted using FIJI/ImageJ (Schindelin *et al.*, 2012; Rueden *et al.*, 2017). To clarify focal adhesion clusters, paxillin or vinculin images were processed with a median filter (0.5 pixels) and a rolling ball background subtraction (12 pixels). To measure ppMLC density along ventral SFs, a line was drawn along a ventral SF between focal adhesions. The intensities along the line in the ppMLC channel were integrated and normalized to the phalloidin integrated intensity. To measure α-actinin-1 intensity, a line was drawn over a ventral SF (including both FAs), and the intensity was measured along that line. FA ends of the ventral SFs were delineated by the phosphorylated-paxillin (pPaxillin) intensity. If necessary, images were stitched together using the Pairwise Stitching plug-in in ImageJ (Preibisch *et al.*, 2009). Kymographs were generated by drawing a one-pixel line along the ablated fiber and taking a reslice. Time-lapse movies were registered using the Template Matching plug-in (Tseng *et al.*, 2011).

To verify that palladin or mDia2 KD resulted in the expected reduction of dorsal SFs or transverse arcs, the number of dorsal SFs along an arc drawn over the curved edge of the crossbow and the number of transverse arcs along a line drawn from the center point of the arc to the innermost transverse arc were quantified. These counts were then divided by the length of the arc or line to obtain the dorsal SF or transverse arc density.

Stress fiber retraction

For SF ablation studies, images were acquired every 1.24 s for 77 s or 155 s. The *xy* coordinates of the two severed ends of the SF were manually tracked in ImageJ. The coordinates were used to calculate the half-distance between the severed ends to measure the retraction of one of the severed ends. The half-distance versus time curve was fitted to the following equation using the curvefit function in MATLAB:

$$L(t) = L_0\left(1-\exp\left(-\frac{t}{\tau}\right)\right)+D_a$$

where L_0 is the stored elastic energy of prestress of the fiber, τ is the viscoelastic time constant, and D_a is the fitted length of the fiber destroyed during ablation (Kumar *et al.*, 2006).

Retraction curves were classified as KV if the fitted curves met all of the following criteria: 1) adjusted $R^2 > 0.9$, 2) viscoelastic time constant $\tau < 0.8$ * imaging window (i.e., $\tau < 61$ s or < 124 s), and 3) sum of squared errors of prediction <10. Retractions that failed to meet any of these criteria were classified as non-KV. Retractions were classified as non-KV/linear if the adjusted R^2 was >0.9 for a fitted line.

Statistical analysis

Statistical analyses and graph generation were performed in GraphPad Prism (v 7.00) or using an online calculator in the case of the Fisher Exact test. Samples were determined to be nonnormal though the Shapiro–Wilk normality test. Nonparametric Kruskal–Wallis tests, followed by a post-hoc Dunn's test for multiple comparisons, were used to assess statistical differences in continuous data sets. In box plots, the top, middle, and bottom of the box represent the 75th, 50th (median), and 25th percentiles, respectively. Bars extend to the 10th and 90th percentiles, and the cross depicts the average. The chi-square test, or the Fisher Exact test if the data set did not meet the requirement for the former, was used to assess differences in the number of KV versus non-KV SFs.

ACKNOWLEDGMENTS

Research reported in this publication was supported by the National Institutes of Health (NIH) under award numbers F31GM119329 (S.L.), R01GM122375 (S.K.), and R21EB016359 (S.K.); the Howard Hughes Medical Institute (HHMI) International Student Research Fellowship (E.K.); and the Siebel Scholars Program (E.K.). The content is solely the responsibility of the authors and does not necessarily represent the official views of the funding agencies. Laser ablation and confocal images were obtained at the CIRM/QB3 Shared Stem Cell Facility. Flow cytometry was conducted at the CRL Flow Cytometry Facility. Micropatterns were fabricated at the QB3 Biomolecular Nanotechnology Center. Structured illumination microscopy was performed at the UC Berkeley Biological Imaging Facility, which was supported in part by the NIH S10 program under award number 1S10(D018136-01). Western blots were imaged using equipment shared by the David Schaffer lab. We thank Mary West, Hector Nolla, Paul Lum, Jessica P. Lee, Kelsey Springer, and Denise Schichnez for training and/or assistance.

REFERENCES

Azatov M, Goicoechea SM, Otey CA, Upadhyaya A (2016). The actin crosslinking protein palladin modulates force generation and mechanosensitivity of tumor associated fibroblasts. Sci Rep 6, 28805.

Blanchoin L, Boujemaa-Paterski R, Sykes C, Plastino J (2014). Actin dynamics, architecture, and mechanics in cell motility. Physiol Rev 94, 235–263.

Burnette DT, Shao L, Ott C, Pasapera AM, Fischer RS, Baird MA, Der Loughian C, Delanoe-Ayari H, Paszek MJ, Davidson MW, *et al.* (2014). A contractile and counterbalancing adhesion system controls the 3D shape of crawling cells. J Cell Biol 205, 83–96.

Burridge K, Guilluy C (2016). Focal adhesions, stress fibers and mechanical tension. Exp Cell Res 343, 14–20.

Burridge K, Wittchen ES (2013). The tension mounts: stress fibers as force-generating mechanotransducers. J Cell Biol 200, 9–19.

Carpi N, Piel M, Azioune A, Fink J (2011). Micropatterning on glass with deep UV. Protoc Exch, doi: 10.1038/protex.2011.238.

Caspani EM, Echevarria D, Rottner K, Small JV (2006). Live imaging of glioblastoma cells in brain tissue shows requirement of actin bundles for migration. Neuron Glia Biol 2, 105.

Chang C, Kumar S (2015). Differential contributions of nonmuscle myosin II isoforms and functional domains to stress fiber mechanics. Sci Rep 5, 13736.

Chang C-W, Kumar S (2013). Vinculin tension distributions of individual stress fibers within cell-matrix adhesions. J Cell Sci 126, 3021–3030.

Chrzanowska-Wodnicka M (1996). Rho-stimulated contractility drives the formation of stress fibers and focal adhesions. J Cell Biol 133, 1403–1415.

Colombelli J, Besser A, Kress H, Reynaud EG, Girard P, Caussinus E, Haselmann U, Small JV, Schwarz US, Stelzer EHK (2009). Mechanosensing in actin stress fibers revealed by a close correlation between force and protein localization. J Cell Sci 122, 1665–1679.

Cramer LP, Siebert M, Mitchison TJ (1997). Identification of novel graded polarity actin filament bundles in locomoting heart fibroblasts: implications for the generation of motile force. J Cell Biol 136, 1287–1305.

Dixon RDS, Arneman DK, Rachlin AS, Sundaresan NR, Costello MJ, Campbell SL, Otey CA (2008). Palladin is an actin cross-linking protein that uses immunoglobulin-like domains to bind filamentous actin. J Biol Chem 283, 6222–6231.
Doyle AD, Wang FW, Matsumoto K, Yamada KM (2009). One-dimensional topography underlies three-dimensional fibrillar cell migration. J Cell Biol 184, 481–490.
Friedl P, Gilmour D (2009). Collective cell migration in morphogenesis, regeneration and cancer. Nat Rev Mol Cell Biol 10, 445–457.
Friedl P, Wolf K (2003). Tumour-cell invasion and migration: diversity and escape mechanisms. Nat Rev Cancer 3, 362–374.
Gateva G, Tojkander S, Koho S, Carpen O, Lappalainen P (2014). Palladin promotes assembly of non-contractile dorsal stress fibers through VASP recruitment. J Cell Sci 127, 1887–1898.
Grooman B, Fujiwara I, Otey C, Upadhyaya A (2012). Morphology and viscoelasticity of actin networks formed with the mutually interacting crosslinkers: palladin and alpha-actinin. PLoS One 7, e42773.
Gupton SL, Eisenmann K, Alberts AS, Waterman-Storer CM (2007). mDia2 regulates actin and focal adhesion dynamics and organization in the lamella for efficient epithelial cell migration. J Cell Sci 120, 3475–3487.
Hayes AJ, Benjamin M, Ralphs JR (1999). Role of actin stress fibres in the development of the intervertebral disc: cytoskeletal control of extracellular matrix assembly. Dev Dyn 215, 179–189.
Hotulainen P, Lappalainen P (2006). Stress fibers are generated by two distinct actin assembly mechanisms in motile cells. J Cell Biol 173, 383–394.
Ikebe M, Koretz J, Hartshorne DJ (1988). Effects of phosphorylation of light chain residues threonine 18 and serine 19 on the properties and conformation of smooth muscle myosin. J Biol Chem 263, 6432–6437.
Ingber DE (2003). Tensegrity I. Cell structure and hierarchical systems biology. J Cell Sci 116, 1157–1173.
Kassianidou E, Brand CA, Schwarz US, Kumar S (2017a). Geometry and network connectivity govern the mechanics of stress fibers. Proc Natl Acad Sci USA 114, 2622–2627.
Kassianidou E, Hughes JH, Kumar S (2017b). Activation of ROCK and MLCK tunes regional stress fiber formation and mechanics via preferential myosin light chain phosphorylation. Mol Biol Cell 28, 3832–3843.
Kassianidou E, Kumar S (2015). A biomechanical perspective on stress fiber structure and function. Biochim Biophys Acta 1853, 3065–3074.
Kumar S, Maxwell IZ, Heisterkamp A, Polte TR, Lele TP, Salanga M, Mazur E, Ingber DE (2006). Viscoelastic retraction of single living stress fibers and its impact on cell shape, cytoskeletal organization, and extracellular matrix mechanics. Biophys J 90, 3762–3773.
Leal-Egaña A, Letort G, Martiel J-L, Christ A, Vignaud T, Roelants C, Filhol O, Théry M (2017). The size-speed-force relationship governs migratory cell response to tumorigenic factors. Mol Biol Cell 28, 1612–1621.
Lee JP, Kassianidou E, MacDonald JI, Francis MB, Kumar S (2016). N-terminal specific conjugation of extracellular matrix proteins to 2-pyridinecarboxaldehyde functionalized polyacrylamide hydrogels. Biomaterials 102, 268–276.
Lee S, Kumar S (2016). Actomyosin stress fiber mechanosensing in 2D and 3D. F1000Research 5, 2261.
Machesky LM, Hall A (1997). Role of actin polymerization and adhesion to extracellular matrix in rac- and rho-induced cytoskeletal reorganization. J Cell Biol 138, 913–926.
Moffat J, Grueneberg DA, Yang X, Kim SY, Kloepfer AM, Hinkle G, Piqani B, Eisenhaure TM, Luo B, Grenier JK, *et al*. (2006). A lentiviral RNAi library for human and mouse genes applied to an arrayed viral high-content screen. Cell 124, 1283–1298.
Oakes PW, Beckham Y, Stricker J, Gardel ML (2012). Tension is required but not sufficient for focal adhesion maturation without a stress fiber template. J Cell Biol 196, 363–374.
Otey CA, Carpen O (2004). a-actinin revisited: a fresh look at an old player. Cell Motil Cytoskel 58, 104–111.
Owen LM, Adhikari AS, Patel M, Grimmer P, Leijnse N, Kim MC, Notbohm J, Franck C, Dunn AR (2017). A cytoskeletal clutch mediates cellular force transmission in a soft, three-dimensional extracellular matrix. Mol Biol Cell 28, 1959–1974.
Parast MM, Otey CA (2000). Characterization of palladin, a novel protein localized to stress fibers and cell adhesions. J Cell Biol 150, 643–656.
Preibisch S, Saalfeld S, Tomancak P (2009). Globally optimal stitching of tiled 3D microscopic image acquisitions. Bioinformatics 25, 1463–1465.
Rönty M, Taivainen A, Moza M, Otey CA, Carpén O (2004). Molecular analysis of the interaction between palladin and α-actinin. FEBS Lett 566, 30–34.
Rueden CT, Schindelin J, Hiner MC, DeZonia BE, Walter AE, Arena ET, Eliceiri KW (2017). ImageJ2: ImageJ for the next generation of scientific image data. BMC Bioinformatics 18, 529.
Schindelin J, Arganda-Carreras I, Frise E, Kaynig V, Longair M, Pietzsch T, Preibisch S, Rueden C, Saalfeld S, Schmid B, *et al*. (2012). Fiji: an open-source platform for biological-image analysis. Nat Methods 9, 676–682.
Sjöblom B, Salmazo A, Djinović-Carugo K (2008). α-Actinin structure and regulation. Cell Mol Life Sci 65, 2688–2701.
Small JV, Rottner K, Kaverina I, Anderson KI (1998). Assembling an actin cytoskeleton for cell attachment and movement. Biochim Biophys Acta 1404, 271–281.
Soiné JRD, Brand CA, Stricker J, Oakes PW, Gardel ML, Schwarz US (2015). Model-based traction force microscopy reveals differential tension in cellular actin bundles. PLoS Comput Biol 11, e1004076.
Tanner K, Boudreau A, Bissell MJ, Kumar S (2010). Dissecting regional variations in stress fiber mechanics in living cells with laser nanosurgery. Biophys J 99, 2775–2783.
Tee YH, Shemesh T, Thiagarajan V, Hariadi RF, Anderson KL, Page C, Volkmann N, Hanein D, Sivaramakrishnan S, Kozlov MM, *et al*. (2015). Cellular chirality arising from the self-organization of the actin cytoskeleton. Nat Cell Biol 17, 445–457.
Théry M, Pépin A, Dressaire E, Chen Y, Bornens M (2006). Cell distribution of stress fibres in response to the geometry of the adhesive environment. Cell Motil Cytoskel 63, 341–355.
Tojkander S, Gateva G, Husain A, Krishnan R, Lappalainen P (2015). Generation of contractile actomyosin bundles depends on mechanosensitive actin filament assembly and disassembly. Elife 4, e06126.
Tojkander S, Gateva G, Schevzov G, Hotulainen P, Naumanen P, Martin C, Gunning PW, Lappalainen P (2011). A molecular pathway for myosin II recruitment to stress fibers. Curr Biol 21, 539–550.
Tseng Q, Wang I, Duchemin-Pelletier E, Azioune A, Carpi N, Gao J, Filhol O, Piel M, Théry M, Balland M (2011). A new micropatterning method of soft substrates reveals that different tumorigenic signals can promote or reduce cell contraction levels. Lab Chip 11, 2231.
Vallenius T (2013). Actin stress fiber subtypes in mesenchymal migrating cells. Open Biol 3, 130001.
Vicente-Manzanares M, Horwitz AR (2010). Myosin light chain mono- and diphosphorylation differentially regulate adhesion and polarity in migrating cells. Biochem Biophys Res Commun 402, 537–542.
Vicente-Manzanares M, Koach MA, Whitmore L, Lamers ML, Horwitz AF (2008). Segregation and activation of myosin IIB creates a rear in migrating cells. J Cell Biol 183, 543–554.
Vicente-Manzanares M, Ma X, Adelstein RS, Horwitz AR (2009). Non-muscle myosin II takes centre stage in cell adhesion and migration. Nat Rev Mol Cell Biol 10, 778–790.
Vicente-Manzanares M, Newell-Litwa K, Bachir AI, Whitmore LA, Horwitz AR (2011). Myosin IIA/IIB restrict adhesive and protrusive signaling to generate front–back polarity in migrating cells. J Cell Biol 193, 381–396.